LETTER • **OPEN ACCESS**

Impact of environment on dynamics of exciton complexes in a WS_2 monolayer

To cite this article: Tomasz Jakubczyk *et al* 2018 *2D Mater.* **5** 031007

2D Materials

OPEN ACCESS

RECEIVED
4 January 2018

REVISED
13 March 2018

ACCEPTED FOR PUBLICATION
6 April 2018

PUBLISHED
30 April 2018

LETTER

Impact of environment on dynamics of exciton complexes in a WS_2 monolayer

Tomasz Jakubczyk[1,5], Karol Nogajewski[2,3], Maciej R Molas[2,3], Miroslav Bartos[2], Wolfgang Langbein[4], Marek Potemski[2,3] and Jacek Kasprzak[1]

[1] Université Grenoble Alpes, CNRS, Grenoble INP, Institut Néel, 38000 Grenoble, France
[2] Laboratoire National des Champs Magnétiques Intenses, CNRS-UGA-UPS-INSA-EMFL, 25 Av. des Martyrs, 38042 Grenoble, France
[3] Faculty of Physics, University of Warsaw, ul. Pasteura 5, 02-093 Warszawa, Poland
[4] School of Physics and Astronomy, Cardiff University, The Parade, Cardiff CF24 3AA, United Kingdom
[5] Present address: Department of Physics, University of Basel, 4056 Basel, Switzerland

E-mail: tomasz.jakubczyk@unibas.ch **and** jacek.kasprzak@neel.cnrs.fr

Keywords: WS_2, transition metal dichalcogenides, exciton dynamics, four wave mixing, valley coherence

Supplementary material for this article is available online

Abstract

Scientific curiosity to uncover original optical properties and functionalities of atomically thin semiconductors, stemming from unusual Coulomb interactions in the two-dimensional geometry and multi-valley band structure, drives the research on monolayers of transition metal dichalcogenides (TMDs). While recent works ascertained the exotic energetic schemes of exciton complexes in TMDs, we here infer their unusual coherent dynamics occurring on subpicosecond time scale. The dynamics is largely affected by the disorder landscape on the submicron scale, thus can be uncovered using four-wave mixing in the frequency domain, which enables microscopic investigations and imaging. Focusing on a WS_2 monolayer, we observe that exciton coherence is lost primarily due to interaction with phonons and relaxation processes towards optically dark excitonic states. Notably, when temperature is low and disorder weak, excitons large coherence volume results in enhanced oscillator strength, allowing to reach the regime of radiatively limited dephasing. Additionally, we observe long valley coherence for the negatively charged exciton complex. We therefore elucidate the crucial role of exciton environment in the TMDs on its dynamics and show that revealed mechanisms are ubiquitous within this family.

1. Introduction

In spite of their illusory academic simplicity, synthetic two-dimensional (2D) materials—such as graphene, black phosphorous, and transition metal dichalcogenides (TMDs)—display stunning properties, which are also revealed in their optical responses. For instance, in monolayers (MLs) of TMDs, the reduced dielectric screening and 2D carrier confinement give rise to exotic, non-hydrogenic excitons with binding energies exceeding 0.2 eV [5], which is an asset enhancing light-matter interaction. The latter is manifested by a strong absorption and subpicosecond population lifetime, favoring formation of surface plasmon polaritons [45] and exciton-polaritons [7, 22, 23] with a valley degree of freedom—to name a few examples illustrating a technology-driven progress in the optics of TMDs. However, there is a need for an in-depth understanding of fundamental mechanisms governing exciton radiative and nonradiative recombination rates in various experimental settings. There is a large spread of reported values of exciton coherence and population decay [29] and little is known about their dependence on microscopic material properties and environmental factors, such as temperature, strain, dielectric surrounding and excitonic disorder on different length scales. The latter generates inhomogeneous broadening, characterized by its spectral full width at half maximum (FWHM) σ.

The main obstacle to access this information, was a large size of the optically probed areas (typically, diameter of a few tens of micron), which are required to implement traditional approaches of nonlinear spectroscopy—such as angle-resolved four-wave mixing (FWM)—inferring decay times of populations and coherent polarizations in extended samples. We here overcome this difficulty, by exploiting phase-sensitive

heterodyne detection. The latter permits to perform FWM spectroscopy in a microscopy configuration, attaining spatial resolution of 300 nm. Using a tungsten disulphide (WS_2) ML, exhibiting the strongest optical activity among all other TMD MLs [21] we observe a giant FWM response of the resonantly generated excitons and we carry out the mapping of their dephasing time ($T_2 = 2\hbar/\gamma$, where γ denotes homogeneous broadening (FWHM)), population decay time T_1 and σ. We further infer the dephasing induced by phonons, by performing FWM temperature dependence.

Additionally, two distinct types of negative trions, i.e. bound states of one hole and two electrons in a globally anti-symmetrical configuration with respect to the combination of their spin and valley index [6], are unambiguously identified in FWM. We show that a single electron is the ground state for optically active trions, where the additional electron and hole are within the same valley as this ground state electron (intra-valley trion), or in the opposite valley (inter-valley trion). An energetic splitting between these states due to exchange interaction was recently predicted [43], and observed for WSe_2 [6, 18, 41] and for WS_2 [31]. We observe the Raman quantum beats [9, 24] resulting from this splitting, revealing coupling between both types of trions. We employ this phenomenon to measure the decay of the trion-valley coherence T_2^{valley} [11, 13, 17, 42], which appears to be significantly longer than previously reported.

2. Methods

We employ the FWM micro-spectroscopy setup [10, 16, 20], adapted to the visible spectral range. First, we use an optical parametric oscillator (Inspire 50 by Radiantis pumped by Tsunami Femto by Spectra-Physics) to create a triplet of short laser pulses around 600 nm: $\mathcal{E}_1$, $\mathcal{E}_2$ and $\mathcal{E}_3$, with adjustable delays τ_{12} and τ_{23}, as depicted in the supplementary figure S1 (stacks.iop.org/TDM/5/031007/mmedia). The three beams are injected co-linearly into the microscope objective (Olympus VIS, NA = 0.6), installed on a XYZ piezo stage. They are focused down to the diffraction limit of 0.6 μm, onto the sample placed in a helium-flow cryostat. $\mathcal{E}_{1,2,3}$ are pre-chirped by using a geometrical pulse shaping [10], so as to attain close to Fourier-limited, 120 fs pulses on the sample. The WS_2 ML flake was mechanically exfoliated from a bulk crystal purchased from HQ-graphene and deposited on a 90 nm thick SiO_2 substrate. The FWM generated within the sub-wavelength (approximately half of the waist) area, diffracts in all directions. There is therefore no k-vector matching condition, on which most FWM experiments rely on. Instead, our microscopy approach imposes the signal to be selected in phase, by performing optical heterodyning. By employing acousto-optic deflectors operating at different radio-frequencies $\Omega_{1,2,3}$, the phases within the pulse trains $\mathcal{E}_{1,2,3}$ are modulated by $n\Omega_{1,2,3}/\nu$, where ν and n denote the laser repetition rate and pulse index within the train, respectively. As a result, the FWM polarization—which in the lowest, third-order is proportional to $\mu^4\mathcal{E}_1{}^\star\mathcal{E}_2\mathcal{E}_3$—evolves with the phase $n(\Omega_3 + \Omega_2 - \Omega_1)/\nu$. This specific phase-drift is locked onto the reference pulse $\mathcal{E}_R$, overlayed with the reflected light, and thus producing a stationary interference with the FWM field. The background-free interference [20] is spectrally dispersed by an imaging spectrometer (Acton, 750 mm focal length) and detected on a CCD camera (Princeton Instruments, Pixis 400 eXcelon).

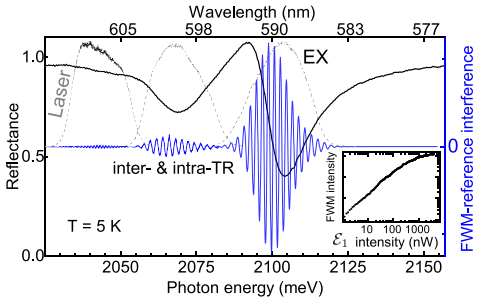

Figure 1. Four-wave mixing micro-spectroscopy of a WS_2 monolayer. Spectrally-resolved reflectance and FWM-reference interference at $\tau_{12} = 0.2$ ps centered at exciton (EX), trion (TR) transitions and the third (trionic) transition. The corresponding spectra of the excitation laser are given by gray dashed lines. Inset: FWM intensity dependence of EX.

3. Results

3.1. Spectral characteristics and exciton coherent dynamics

We first perform micro-reflectance from a flake, to identify exciton (EX) and trion (TR) transitions, as shown in figure 1. As discussed in more detail further (see figure 4), we unambiguously confirm the presence of two types of trions: inter- and intra-valley trions [31, 38]. To probe their coherence and population density dynamics we employ the FWM micro-spectroscopy setup described above. We probe the flake with the $\mathcal{E}_{1,2,3}$ pulsed laser beams which are spectrally centered at either EX (~590 nm) or TR (~600 nm), with a bandwidth about 7 nm (FWHM). The reference $\mathcal{E}_R$ beam is focused on the surrounding SiO_2, so that its lineshape is not affected by a strong absorption of the flake. Figure 1 presents the resulting FWM spectral interferograms obtained on both resonances in the WS_2 flake at T = 5 K. We note that the amplitude of the TR is typically an order of magnitude weaker than the EX's one. Below the TR line, around 2040 meV we further retrieve FWM of another type of valley-trion [26]. No other transitions have been detected in reflectance or FWM within the spectral range (530–650) nm. As a resonant multi-pulse technique, FWM is suited to reveal biexciton transitions [12]. Yet, no signatures of the latter have been detected here. The fringe period in figure 1 is given by a delay of 2 pico-

seconds (ps) between the reference pulse $\mathcal{E}_R$ and the last arriving pulse, triggering the FWM emission. Its intensity and phase are retrieved by applying spectral interferometry. The former as a function of $\mathcal{E}_1$ intensity is shown in the inset, yielding the limit of the third-order $\chi^{(3)}$ regime (where further experiments are performed) up to around 100 nW. It is worth to note that FWM can be readily detected with $\mathcal{E}_1$ as low as 1 nW, generating a low carrier density of a few 10^8 cm^{-2}. When exciting stronger than 100 nW, FWM visibly starts to saturate. Interestingly, we also observe that, even at this low exciton density, there is a bleaching and energy blueshift of the exciton reflectance, as presented in supplementary figure S2. While we refrain here from the definite interpretation of such a strikingly nonlinear power dependence, we note that the same effect has been recently observed in a $MoSe_2$-based heterostructure [36]. In WS_2 MLs, the optically active exciton (EX) has a larger transition energy than the dark one [25, 40, 44], such that at low temperature the PL of EX is suppressed [31], as shown in the supplementary figure S3. While this issue remains relevant in view of competing relaxation channels of the bright exciton, it is not an obstacle to drive its FWM: EX are resonantly and selectively created, generating a giant response, owing to the μ^4 scaling of the FWM, where μ is the oscillator strength.

The EX spectral lineshape measured in reflectance (figure 1) is dominated by inhomogeneous broadening with a Gaussian distribution of around 15 meV (FWHM). FWM spectroscopy has been conceived primarily to access the homogeneous broadening γ in an inhomogeneously broadened ensemble, exhibiting a spectral FWHM σ. The complex conjugate in the FWM definition, imposes phase conjugation between the first-order polarization induced by $\mathcal{E}_1$ and the FWM. For $\tau_{12} > \hbar/\sigma$, its transient appears as a Gaussian, known as a photon echo. It is centered at $t = \tau_{12}$ and has a FWHM, corrected with respect to the pulse duration, equal to $8\ln(2)\hbar/\sigma$. Formation of such an echo is illustrated in figure 2(a), where time-resolved FWM amplitude of EX versus τ_{12} is shown. The echo develops during the initial $0 < \tau_{12} < 0.5$ ps. By inspecting FWM for later delays, for example $\tau_{12} = 0.7$ ps (orange trace) we retrieve inhomogeneous width σ of around 11 meV (FWHM).

Time-integrated amplitudes of the photon echo as a function of τ_{12} for different temperatures are reported in figure 2(b). Here, the decay reflects γ. To retrieve γ, the data are fitted with an exponential decay $\exp(-\gamma\tau_{12}/\hbar)$, convoluted with a Gaussian to account for a pulse duration of 0.12 ps. At T = 5 K we obtain $\gamma_{EX} = (2.1 \pm 0.1)$ meV, yielding dephasing time $T_2 = (620 \pm 20)$ fs. Thus EX in WS_2 shows a larger homogenous width than its counterpart in recently investigated $MoSe_2$ MLs [16], in line with a superior linear absorption in WS_2 with respect to $MoSe_2$ [21]. The temperature dependence of γ is illustrated in figure 2(c). The data are modeled [33] (purple trace) with the following equation: $\gamma(T) = \gamma_0 + aT + b/[\exp(E_1/k_BT) - 1]$. Besides the constant contribution $\gamma_0 = (2.1 \pm 0.1)$ meV, the linear coefficient $a = (18 \pm 3)\,\mu$eV K^{-1} is attributed to low energy acoustic phonons. The latter term, with the $b = (32 \pm 6)$ meV, is due to thermal activation of optical phonons with dominant or mean energy $E_1 = (37 \pm 3)$ meV, which indeed supply a large density of states above 300 cm$^{-1} \simeq 37$ meV [27]. The phonon dephasing mechanisms are therefore similar as in $MoSe_2$ MLs [16] and as in semiconductor quantum wells [3]. Above T = 210 K, the FWM decay is limited by the temporal resolution, such that γ cannot be extracted, although a strong FWM is measured up to the room temperature.

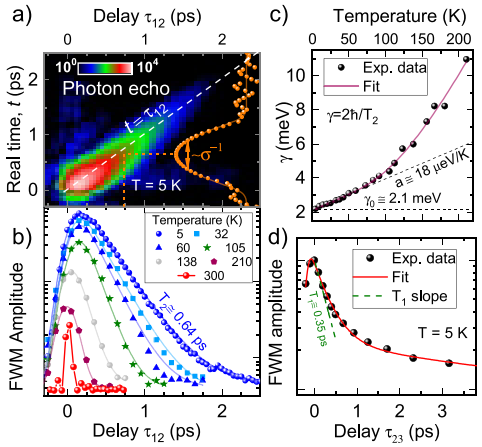

Figure 2. Exciton dephasing in WS_2 ML measured in two-beam FWM. (a) Time-resolved FWM showing the photon echo at T = 5 K, σ is retrieved from its temporal width (orange trace): the measured FWHM is 0.45 ps and correcting with respect to the pulse duration of 0.12 ps yields the actual echo width of 0.33 ps (FWHM). Logarithmic color scale. (b) Time-integrated echo with model fits as a function of delay τ_{12} for temperatures, as indicated. The non-exponential behavior is due to a constant offset, giving a noise level. (c) The retrieved homogeneous broadening versus temperature γ(T) fitted with model described in the text, solid red. The dashed lines represent parameters obtained from the fit. (d) Exemplary measurement of the EX density dynamics for a given position. The initial decay T_1 is mainly due to radiative recombination T_{rad} and non-radiative relaxation T_{dark} to the EX dark state, such that $(T_1)^{-1} = (T_{rad})^{-1} + (T_{dark})^{-1}$.

A representative measurement of the population dynamics (spectrally-integrated FWM amplitude versus τ_{23}) via three-beam FWM [10, 16] is shown in figure 2(d). The measurement was performed at the same spot as the dephasing study, presented in figure 2. The population dynamics is dominated by an initial exponential decay with a constant of $T_1 \simeq 0.35$ ps, followed by a longer dynamics described by two additional exponential decays [35] ($T^A_{slow} \simeq 4.7$ ps and $T^B_{slow} \simeq 46$ ps) that we can relate to phase space distribution via scattering processes and scattering back from the exciton dark ground state. We note that the portion of secondary excitons, decaying on a nanosecond timescale, is at least an order of magnitude

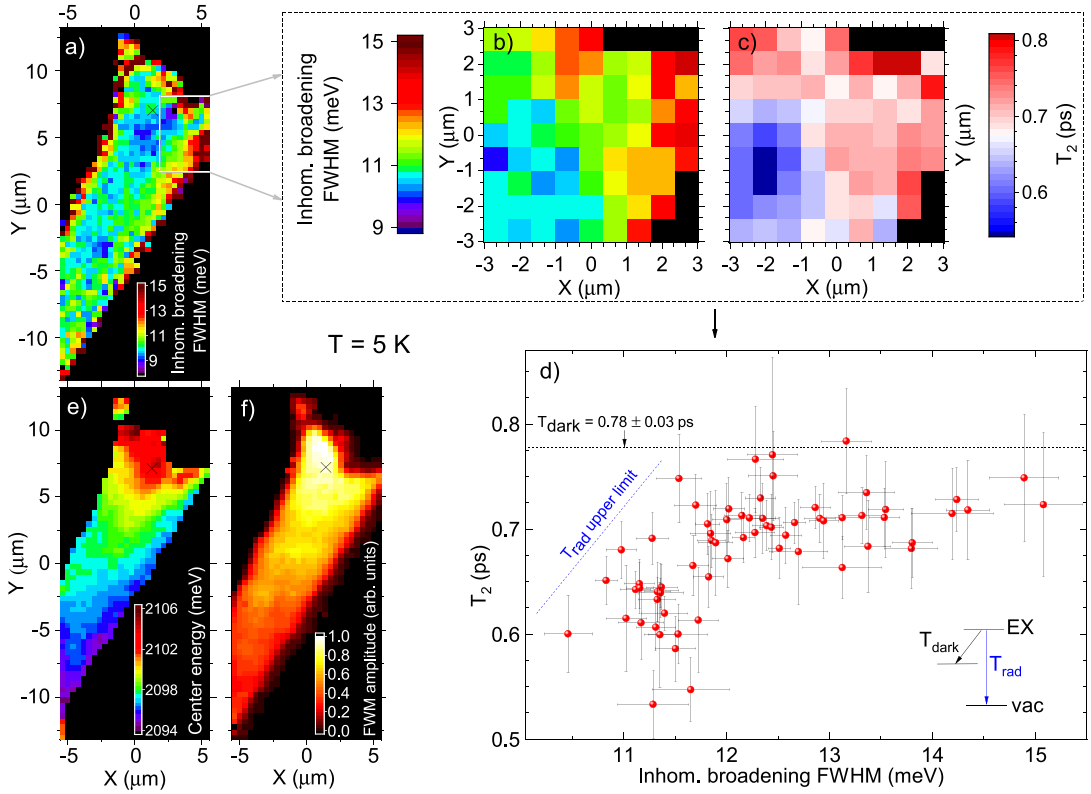

Figure 3. Spatially-resolved probing of EX coherence in a WS_2 ML via FWM hyperspectral imaging. (a) Spatial imaging of the inhomogeneous broadening σ retrieved from time-resolved FWM at $\tau_{12} = 0.6$ ps. Zoomed map of (b) inhomogeneous broadening and (c) dephasing time. (d) Correlation between homogeneous and inhomogeneous broadenings, indicating radiative rate governed by localization via disorder and illustrating competition between radiative recombination and non-radiative EX shuffling to its dark state (sketched). The dashed black line indicates T_{dark} extracted from a fit (see the supporting information). (e) Hyperspectral FWM imaging, $\tau_{12} = 0.2$ ps, hue indicates transition energy. (f) Time-integrated FWM amplitude reflecting μ, linear scale over an order of magnitude. The black cross indicates location where results presented on figures 2 and 4 were obtained.

larger than on recently studied $MoSe_2$ MLs. This we associate with a dark exciton ground state in WS_2 and its bright character in $MoSe_2$ [25].

The obtained result ($T_2 \simeq 2T_1$) indicates that dephasing is mainly due to the population decay, which we attribute to be due primarily to the fast radiative recombination. Indeed, excitons in ML TMDs possess the radiative lifetime T_{rad} of a few hundred femto-seconds, as recently revealed via two-colour pump-probe [32], FWM [16, 28] and TMD polaritons studies [7, 22, 23]—all these results signify a large EX transition dipole moment and coherence volume spanning across many Bohr radii [8]. The parameter T_{dark} describing phase space distribution via scattering processes and relaxation to the dark exciton ground state is also expected to contribute to the fast initial decay. Other nonradiative recombination processes are expected to be of minor impact, as they are not faster than the decay of secondary excitons, that is $\geqslant$46 ps (we assume that these processes have the same dynamics for both bright and dark excitons). We also note a weak role of phonons on the excitons dynamics in this low temperature range (see figure 2(c)). To get a comprehensive view of the possible mechanisms influencing the exciton dynamics, the local insight into σ, T_2, population decay and μ is required, and should be strengthen by imaging of these quantities across the entire flake. Crucially, such an original capability is offered by the heterodyne FWM microscopy. Thus, we now focus on the FWM mappings and analyze spatial correlations between the above parameters.

3.2. FWM mappings

In the first step, we focus on spatial variation of σ. We therefore acquire FWM spectral interferograms at $\tau_{12} = 0.6$ ps and retrieve time-resolved FWM amplitude of EX, while scanning over the flake surface. For each location, we inspect the width of the photon echo, from which we measure σ. The result is shown in figure 3(a). In the middle of the flake, we identify regions of a smaller inhomogeneous broadening, down to 9 meV (FWHM), yet still largely dominating over γ. It is worth to note, that the largest σ, and thus most pronounced exciton localization, is measured at the borders of the flake. This is related to the strain gradients and variations of the dielectric screening by the substrate, which are expected to be strong along the edges. These locations are preferential for wrinkling, local deformations and lattice defects creating deep potential centers trapping individual emitters (see supplementary figure S3(d)). As an origin of σ, we point toward a local strain and charges trapped on a

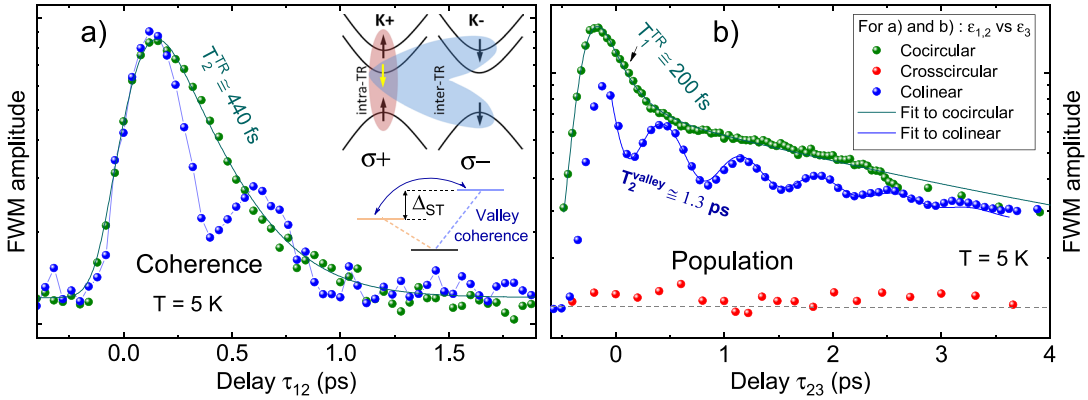

Figure 4. FWM of the intra- and inter-valley trions in a WS_2 ML. (a) Trion coherence dynamics measured in co-circular (green) and co-linear (blue) polarizations of $\mathcal{E}_{1,2,3}$. Inset: Intra-TR in K+ valley and inter-TR in K− valley are Raman-coupled by sharing the same ground state (yellow electron, symbolized with a down-arrow). (b) Population dynamics measured in co-circular and co-linear polarizations of $\mathcal{E}_{1,2,3}$. Semi-transparent traces are the fitted dynamics. For the cross-circular setting of $\mathcal{E}_{1,2}$ and $\mathcal{E}_3$ the measured FWM is at the noise level (gray dashed line), indicating a strongly suppressed inter-valley scattering.

flake. We note that a comparable σ was measured using a suspended ML flake of $MoSe_2$ (see supplementary figure S6), excluding the interface roughness between the SiO_2 and the flake as a principal source of inhomogeneity. Newly, it has been found that σ can be suppressed by encapsulating a flake in hexagonal boron nitride [2, 4]: FWM performed on our preliminary *h*BN/WS_2/*h*BN heterostructure indeed has revealed reduction of σ, however its complete cancelation has not been observed (not shown). Moreover, a reduced spectral jitter was measured on non-insulating substrates [15], helping to evacuate trapped charges, further indicating decisive role of charge fluctuation on the amount of inhomogeneous broadening.

In the next step, we focus on the area exhibiting a large variation of σ, marked with a gray rectangle in figure 3(a). Again we perform mappings, this time varying also the delay τ_{12} for each position. Such retrieved T_2 and σ are presented as color-coded maps in figures 3(b) and (c), respectively. Their spatial correlation is striking and emphasized in figure 3(d): the fastest dephasing is measured at the areas of smallest σ. We interpret this as follows. Center of mass of two-dimensional excitons moves within a disordered potential landscape [34], arising from the variation of dielectric contrasts, strain from the substrate, uncontrollable impurities, vacancies, etc. Through the Schrödinger equation, the disorder acts on the wave-function localization in real space and thus results in its delocalization in k-space, modifying radiative rates with respect to free excitons. In other words, the disorder mixes the states inside and outside of the radiative cone, and thus creates a distribution of states with an oscillator strength reduced as compared to ones fully in the radiative cone. Furthermore, it generates the spread of transition energies, adding up to σ. Note, that this localization is weak [37] comparing to localization resulting from deep traps [14], resulting in a distinctive emission band well below the EX emission (see supplementary figure S3). As presented in figure 3(d), T_2 starts to decrease only for a sufficiently low σ, where the radiative decay time T_{rad} becomes fast enough to compete with another channel, identified as the EX relaxation to the dark ground state. Such channel was not observed in $MoSe_2$ displaying a bright exciton ground state (see supplementary figure S4(a)). Conversely, for largest σ, the non-radiative decay dominates, as the T_{rad} is increased through the localization. These spatial correlations, observed on two representatives of the TMDs ML family, demonstrate that radiative rates and dephasing of excitons in this class of materials are governed by exciton localization imposed by a local disorder.

The slope of the transition energy owing to the strain gradient is observed in figure 3(e), where the center transition energy is encoded in a hue level. In figure 3(f) we present time-integrated FWM amplitude of the EX transition (corrected by the excitation lineshape) reflecting μ. Comparing figure 3(f) with figure 3(a), we note that the areas of the smallest σ yield the strongest FWM (see also supplementary figure S4). This is because with decreasing σ (disorder), the spatial overlap between excitons increases, enhancing the EX interaction strength and thus resulting in a more intense time-integrated FWM. We note that the largest oscillator strength is observed in areas with the highest transition energy.

3.3. Trion dynamics

We now turn to investigation of the trion transition (TR) [31]. The latter is formed when an additional electron occupies the lowest conduction band, as depicted in the inset of figure 4(a). Depending on its spin (and valley-index), one can form a singlet state (intra-valley trion, intra-TR) or a triplet-state (inter-valley trion, inter-TR) [6, 31, 38]. To address coherence dynamics of these TR complexes, $\mathcal{E}_{1,2,3}$ are prepared co-circularly, selectively addressing K+ valleys. We investigate it at the same spatial location as for experiments illustrated on figure 2, yielding low σ and

marked with a cross in figures 4(a), (e) and (f). Similarly as for EX, we obtain a single exponential decay yielding the averaged TR dephasing $T_2(\mathrm{TR}) = (440 \pm 10)$ fs. This faster dephasing with respect to EX is attributed to fast TR relaxation into the lower lying dark states, leaving an electron with a varying momentum, and inducing additional dephasing via final state damping.

When $\mathcal{E}_{1,2,3}$ are co-linear, K+ and K− valleys are excited in tandem, as linearly polarized light contains equal amounts of both circularly polarized components. The beats observed in this configuration can only be explained by the existence of two non-degenerate distinct types of trions [6, 31]. Intra-TR in K+ and inter-TR in K− valley share the same ground state corresponding to the presence of an electron in the lowest conduction band, labeled with a yellow down-arrow in the inset in figure 4(a). In other words, the trions form a V-type system, coupled through a common electron acting as a ground state. In such a configuration, $\mathcal{E}_1$ and $\mathcal{E}_2$ generate valley coherence between both types of trions resulting in the Raman quantum beats [9, 24], as sketched in the inset in figure 4(a). Owing to the TR singlet-triplet splitting [31], labeled as Δ_{ST}, the phase of this coherence evolves when increasing τ_{12}. Therefore, the measured coherence dynamics, shown in figure 4(a), displays beating [9] with a period $T_{\mathrm{ST}} \simeq 0.71$ ps, yielding $\Delta_{\mathrm{ST}} = 2\pi\hbar/T_{\mathrm{ST}} = 5.8$ meV. Similar values were retrieved when varying the position on the flake. Note that this singlet-triplet splitting is not resolvable either in reflectance or in the FWM spectrum due to the inhomogeneous broadening present in the studied bare WS_2 monolayer. Clearly, there exist spatial and temporal correlations of spectral fluctuations of the two transitions, so that their relative coherence is maintained long enough to induce the beating of the FWM signal.

To measure the TR density dynamics we perform the τ_{23}-dependence of the FWM [16] for a fixed $\tau_{12} = 0.2$ ps. Once again, via co-circular excitation we selectively probe the intra-TR dynamics. As presented in figure 4(b), it displays a fast monotonous decay, owing to the relaxation into the dark exciton state, followed by a slower revival of the FWM generated by the dark excitons relaxing back into the light cone [16, 35]. This interpretation is strengthened by comparing the TR dynamics in WS_2 with the one measured in $MoSe_2$ ML (see supplementary figure S5), exhibiting optically bright ground state. In the latter case, as the TR recombination leaves an electron with a varying momentum and relaxation to lower energy state is not possible, we observe a substantially longer TR radiative decay with respect to EX.

It is worth pointing out that no FWM is observed (either at TR or EX) for opposite circular polarizations of $\mathcal{E}_{1,2}$ and $\mathcal{E}_3$ pointing towards a particularly robust valley polarization in WS_2 MLs.

Upon co-linear excitation, the initial density dynamics displays again an oscillatory behavior: the first two pulses do not only create the intra-TR and inter-TR populations, but also induce the valley coherence between them, once more generating the Raman quantum beats [9, 24]. All these ingredients contribute to the FWM signals, which we model with a phenomenological fitting curve (see supporting information, section VIII) and extract the valley coherence dephasing time of $T_2^{\mathrm{valley}} = (1.3 \pm 0.2)$ ps. Note that we use this parameter here to describe coherence between two energetically non-degenerate trion states occupying opposite valleys. The obtained value is much longer than previously reported [11, 13, 17, 42]. It is measured on a location with low σ confirming recent reports suggesting that a shallow disorder potential plays a critical role in the exciton valley coherence [39]. For longer delays the valley coherence has dephased, such that the subsequent exciton dynamics is similar for both polarization configuration.

Thus TR singlet and triplet transitions of WS_2 are here unveiled via FWM, generating oscillations of ultrafast dynamics of both coherence and population.

4. Conclusion

To conclude, we demonstrated a giant nonlinear optical response of exciton complexes in WS_2 MLs. The substantial enhancement of the FWM retrieval efficiency with respect to standard semiconductor quantum wells was exploited to unravel the impact of a local disorder in two-dimensional systems onto exciton dynamics and dephasing. The valley degree of freedom was unveiled, when considering the trion structure. Our results indicate that coherent nonlinear microscopy is suited to explore optical properties of emerging optoelectronic and optomechanical [30] devices and heterostructures [4] made of layered semiconductors. Especially, the emerging disorder-free TMD heterostructures, offering exciton transitions operating close to the homogenous limit, should enable to demonstrate long-range propagation of the coherence and of the exciton/polariton diffusion. These aspects, important both from the fundamental and application point of view, could be revealed through the spatially-resolved FWM measurements. An alluring perspective is to image the exciton coherent dynamics on a nanometer areas and to conjugate it with the structural properties of TMDs, which can be revealed down to atomic scale using scanning tunneling microscopy. This could be achieved by transferring our methodology towards the nanoscopic regime [1, 19], offering a spatial resolution of a few tens of nanometers.

Acknowledgments

We acknowledge the financial support by the European Research Council (ERC) Starting Grant PICSEN (grant no. 306387), the ERC Advanced Grant MOMB (grant no. 320590), the EC Graphene Flagship project (No. 604391) and the ATOMOPTO project within the TEAM programme of the Foundation for Polish Science co-financed by the EU within the ERDFund. We also acknowledge the technical support from Nanofab facility of the Institute Néel, CNRS UGA.

ORCID iDs

Tomasz Jakubczyk https://orcid.org/0000-0002-8875-4514
Maciej R Molas https://orcid.org/0000-0002-5516-9415

References

[1] Aeschlimann M, Brixner T, Fischer A, Kramer C, Melchior P, Pfeiffer W, Schneider C, Strüber C, Tuchscherer P and Voronine D V 2011 Coherent two-dimensional nanoscopy *Science* **333** 1723
[2] Ajayi O A *et al* 2017 Approaching the intrinsic photoluminescence linewidth in transition metal dichalcogenide monolayers *2D Mater.* **4** 031011
[3] Borri P, Langbein W, Hvam J M and Martelli F 1999 Well-width dependence of exciton-phonon scattering in $In_xGa_{1-x}As/GaAs$ single quantum wells *Phys. Rev.* B **59** 2215
[4] Cadiz F *et al* 2017 Excitonic linewidth approaching the homogeneous limit in MoS_2 based van der Waals heterostructures: accessing spin-valley dynamics *Phys. Rev.* X **7** 021026
[5] Chernikov A, Berkelbach T C, Hill H M, Rigosi A, Li Y, Aslan O B, Reichman D R, Hybertsen M S and Heinz T F 2014 Exciton binding energy and nonhydrogenic Rydberg series in monolayer WS_2 *Phys. Rev. Lett.* **113** 076802
[6] Courtade E *et al* 2017 Charged excitons in monolayer WSe_2: experiment and theory *Phys. Rev.* B **96** 085302
[7] Dufferwiel S *et al* 2015 Exciton-polaritons in van der Waals heterostructures embedded in tunable microcavities *Nat. Commun.* **6** 8579
[8] Feldmann J, Peter G, Göbel E O, Dawson P, Moore K, Foxon C and Elliott R J 1987 Linewidth dependence of radiative exciton lifetimes in quantum wells *Phys. Rev. Lett.* **59** 2337–40
[9] Ferrio K B and Steel D G 1998 Raman quantum beats of interacting excitons *Phys. Rev. Lett.* **80** 786
[10] Fras F, Mermillod Q, Nogues G, Hoarau C, Schneider C, Kamp M, Höffling S, Langbein W and Kasprzak J 2016 Multi-wave coherent control of a solid state single emitter *Nat. Photon.* **10** 155
[11] Hao K, Moody G, Wu F, Dass C K, Xu L, Chen C-H, Sun L, Li M-Y, Li L-J, MacDonald A H and Li X 2016 Direct measurement of exciton valley coherence in monolayer WSe_2 *Nat. Phys.* **12** 677–82
[12] Hao K *et al* 2017 Neutral and charged inter-valley biexcitons in monolayer $MoSe_2$ *Nat. Commun.* **8** 15552
[13] Hao K *et al* 2017 Trion valley coherence in monolayer semiconductors *2D Mater.* **4** 025105
[14] Hichri A, Ben Amara I, Ayari S and Jaziri S 2017 Exciton center-of-mass localization and dielectric environment effect in monolayer WS_2 *J. Appl. Phys.* **121** 235702
[15] Iff O, He Y-M, Lundt N, Stoll S, Baumann V, Höfling S and Schneider C 2017 Substrate engineering for high-quality emission of free and localized excitons from atomic monolayers in hybrid architectures *Optica* **4** 669–73
[16] Jakubczyk T, Delmonte V, Koperski M, Nogajewski K, Faugeras C, Langbein W, Potemski M and Kasprzak J 2016 Radiatively limited dephasing and exciton dynamics in $MoSe_2$ monolayers revealed with four-wave mixing microscopy *Nano Lett.* **16** 5333
[17] Jones A M *et al* 2013 Optical generation of excitonic valley coherence in monolayer WSe_2 *Nat. Nanotechnol.* **8** 634–8
[18] Jones A M, Yu H, Schaibley J R, Yan J, Mandrus D G, Taniguchi T, Watanabe K, Dery H, Yao W and Xu X 2016 Excitonic luminescence upconversion in a two-dimensional semiconductor *Nat. Phys.* **12** 323–7
[19] Kravtsov V, Ulbricht R, Atkin J M and Raschke M B 2015 Plasmonic nanofocused four-wave mixing for femtosecond near-field imaging *Nat. Nanotechnol.* **11** 459
[20] Langbein W and Patton B 2006 Heterodyne spectral interferometry for multidimensional nonlinear spectroscopy of individual quantum systems *Opt. Lett.* **31** 1151
[21] Li Y, Chernikov A, Zhang X, Rigosi A, Hill H M, van der Zande A M, Chenet D A, Shih E-M, Hone J and Heinz T F 2014 Measurement of the optical dielectric function of monolayer transition-metal dichalcogenides: MoS_2, $MoSe_2$, WS_2, and WSe_2 *Phys. Rev.* B **90** 205422
[22] Liu X, Galfsky T, Sun Z, Xia F, Lin E-C, Lee Y-H, Kéna-Cohen S and Menon V M 2014 Strong light-matter coupling in two-dimensional atomic crystals *Nat. Photon.* **9** 30
[23] Lundt N *et al* 2016 Room-temperature Tamm-plasmon exciton-polaritons with a WSe_2 monolayer *Nat. Commun.* **7** 13328
[24] Mermillod Q *et al* 2016 Dynamics of excitons in individual inas quantum dots revealed in four-wave mixing spectroscopy *Optica* **3** 377
[25] Molas M R, Faugeras C, Slobodeniuk A O, Nogajewski K, Bartos M and Potemski M 2017 Brightening of dark excitons in monolayers of semiconducting transition metal dichalcogenides *2D Mater.* **4** 021003
[26] Molas M R, Nogajewski K, Slobodeniuk A O, Binder J, Bartos M and Potemski M 2017 Optical response of monolayer, few-layer and bulk tungsten disulfide *Nanoscale* **9** 13128–41
[27] Molina-Sánchez A and Wirtz L 2011 Phonons in single-layer and few-layer MoS_2 and WS_2 *Phys. Rev.* B **84** 155413
[28] Moody G *et al* 2015 Intrinsic homogeneous linewidth and broadening mechanisms of excitons in monolayer transition metal dichalcogenides *Nat. Commun.* **7** 8315
[29] Moody G, Schaibley J and Xu X 2016 Exciton dynamics in monolayer transition metal dichalcogenides *J. Opt. Soc. Am.* B **33** C39–49
[30] Morell N, Reserbat-Plantey A, Tsioutsios I, Schädler K G, Dubin F, Koppens F H L and Bachtold A 2016 High quality factor mechanical resonators based on WSe_2 monolayers *Nano Lett.* **16** 5102
[31] Plechinger G, Nagler P, Arora A, Schmidt R, Chernikov A, del Águila A G, Christianen P C, Bratschitsch R, Schüller C and Korn T 2016 Trion fine structure and coupled spin-valley dynamics in monolayer tungsten disulfide *Nat. Commun.* **7** 12715
[32] Poellmann C, Steinleitner P, Leierseder U, Nagler P, Plechinger G, Porer M, Bratschitsch R, Schüller C, Korn T and Huber R 2015 Resonant internal quantum transitions and femtosecond radiative decay of excitons in monolayer WSe_2 *Nat. Mater.* **14** 889
[33] Rudin S, Reinecke T and Segall B 1990 Temperature-dependent exciton linewidths in semiconductors *Phys. Rev.* B **42** 11218
[34] Savona V and Langbein W 2006 Realistic heterointerface model for excitonic states in growth-interrupted GaAs quantum wells *Phys. Rev.* B **74** 075311
[35] Scarpelli L, Masia F, Alexeev E M, Withers F, Tartakovskii A I, Novoselov K S and Langbein W 2017 Resonantly excited exciton dynamics in two-dimensional $MoSe_2$ monolayers *Phys. Rev.* B **96** 045407
[36] Scuri G *et al* 2018 Large excitonic reflectivity of monolayer $MoSe_2$ encapsulated in hexagonal boron nitride *Phys. Rev. Lett.* **120** 037402
[37] Singh A *et al* 2016 Trion formation dynamics in monolayer transition metal dichalcogenides *Phys. Rev.* B **93** 041401

[38] Singh A *et al* 2016 Long-lived valley polarization of intravalley trions in monolayer WSe_2 *Phys. Rev. Lett.* **117** 257402
[39] Tran K, Singh A, Seifert J, Wang Y, Hao K, Huang J-K, Li L-J, Taniguchi T, Watanabe K and Li X 2017 Disorder-dependent valley properties in monolayer WSe_2 *Phys. Rev.* B **96** 041302
[40] Wang G *et al* 2017 In-plane propagation of light in transition metal dichalcogenide monolayers: optical selection rules *Phys. Rev. Lett.* **119** 047401
[41] Wang Z, Zhao L, Mak K F and Shan J 2017 Probing the spin-polarized electronic band structure in monolayer transition metal dichalcogenides by optical spectroscopy *Nano Lett.* **17** 740–6
[42] Ye Z, Sun D and Heinz T F 2017 Optical manipulation of valley pseudospin *Nat. Phys.* **13** 26–9
[43] Yu H, Liu G-B, Gong P, Xu X and Yao W 2014 Dirac cones and dirac saddle points of bright excitons in monolayer transition metal dichalcogenides *Nat. Commun.* **5** 3876
[44] Zhang X X *et al* 2017 Magnetic brightening and control of dark excitons in monolayer WSe_2 *Nat. Nanotechnol.* **12** 883–8
[45] Zhou Y *et al* 2017 Probing dark excitons in atomically thin semiconductors via near-field coupling to surface plasmon polaritons *Nat. Nanotechnol.* **12** 856–60